Nanoscale Modeling of Surface Phenomena in Aluminum Using Machine Learning Force Fields

Published as part of The Journal of Physical Chemistry virtual special issue "Machine Learning in Physical Chemistry".

James Chapman* and Rampi Ramprasad
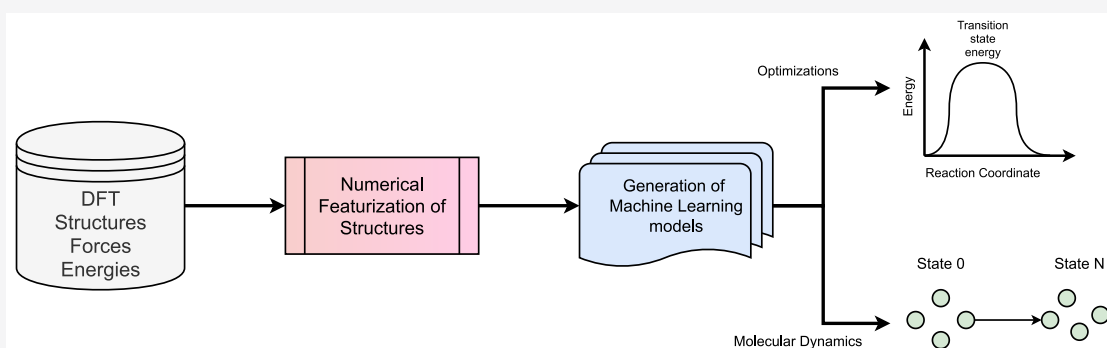
ACCESS | 📊 Metrics & More | 📄 Article Recommendations | 🆂🅸 Supporting Information

ABSTRACT: The study of nanoscale surface phenomena is essential in understanding the physical processes that aid in technologically relevant applications, such as catalysis, material growth, and failure nucleation. While experimental observations, such as those based on various forms of microscopy, can be used to better understand surface diffusion mechanisms, the resulting information is often limited in both its spatial and temporal resolution. Therefore, computational methodologies have become critical in the study of the processes that occur in these domains. Until recently, these methodologies have fallen into two broad categories: quantum mechanics (QM) based methods and semiempirical/classical methods. The former are computationally demanding, but accurate and versatile, while the latter are computationally inexpensive, but are significantly limited in their versatility. Machine learning (ML) methods have shown the potential to bridge these two domains by combining the cost of classical methods with the accuracy of QM. In this work, we employ recently developed ML models to simulate a variety of surface phenomena of aluminum. Adatom diffusion barriers were predicted via nudged elastic band calculations. Surface dynamics were also considered by studying the melting temperature of Al slabs and nanoparticles, along with the epitaxial growth of the Al (110) surface.

■ INTRODUCTION

As the fabrication of materials further pushes into the nano/atomic regime, interest in understanding the fundamental aspects of growth/failure methods for energy storage, catalysis, and/or biomedical applications has greatly increased.[1,2] Therefore, understanding how individual atomic-level processes aid in the observation of macroscopic phenomena is of critical importance. Aluminum and Al-alloys are vital materials for such applications for many reasons, for example, electrical conductivity, recyclability to its original state, respectable corrosion resistance, etc.[3−7] Therefore, understanding how Al is fabricated, as well as how it breaks down, are crucial pieces of information for these applications, as their dependability directly depends on answers to these phenomena.

Atomistic computational techniques have been instrumental in the examination of a multitude of nanoscale materials phenomena.[8−13] These methods have often been placed in one

of two broad domains: QM based methods such as density functional theory (DFT),[14,15] and semiempirical methods such as the embedded atom method.[16−22] However, both classes suffer from several drawbacks. QM methods, while able to predict properties with exceptional accuracy, are computationally burdensome, and considerably limit both the time and length scales that one may probe. Semiempirical/classical methods significantly reduce the time to predict material properties, resulting in the study of large systems over long time-scales. However, such methods generally suffer from
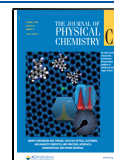
reduced accuracy and transferability, as they are often fit to specific regions of a potential energy surface, and are often not generalizable to new regions.[23]

In an attempt to bridge these domains, data-driven machine learning (ML) methods have become popular due to their ability to reliably retain the accuracy of QM at the cost of semiempirical methods.[24−32] Unlike the previously mentioned computational paradigms, ML methods rely on statistically derived functional forms, rather than those derived from physical intuition. Such models may encounter reduced accuracy when extrapolating to new environments, and will often break down more frequently than classical models. However, these ML approaches offer a variety of advantages, such as the cost required to construct a new model, their accuracy when interpolating between known environments, and their ability to be iteratively and adaptively improved in a systematic manner.[8,33−41]

In this letter, we demonstrate the use of our ML platform, AGNI (Adaptive Generlizable Neighborhood Informed), in predicting a multitude of surface phenomena on aluminum. MD simulations, and nudged elastic band calculations, are utilized to predict a multitude of surface phenomena over many time and length scales. We first begin by providing a short synopsis of the AGNI methodology. We then discuss the diffusion profiles of adatoms on various Al surfaces. Predictions of the melting temperature of Al surfaces, and the size-dependent melting temperature of Al nanoparticles are then shown. Finally, we discuss the expitaxial growth of the Al (110) surface. The compilation of work presented in this manuscript aims to reveal the potential of ML schemes toward the study of surface phenomena over time and length scales far beyond that of QM calculations, bridging the gap between QM and experimental regimes.

■ COMPUTATIONAL DETAILS

AGNI Workflow. The AGNI methodology consists of four key steps: (1) construction of a diverse and representative set of reference data, (2) decomposition of local/structural geometric information to numerical descriptors, (3) training of a ML model given some partition of the aforementioned reference data, and (4) interfacing of the final ML models to a MD engine, capable of simulating the time-evolution of atomistic phenomena. In the following sections we provide a brief synopsis of steps (1), (2), and (3), and we refer the reader to our previous works for a more detailed description.[33−35,40−42]

Atomic-Level Descriptors. An atom's local geometry is decomposed into numerical descriptors that are then mapped to a corresponding property, such as the total potential energy, or atomic forces. These descriptors aim to capture unique aspects of an atom's local atomic environment with features resembling scalar, vector, and tensor quantities. The functional forms of the atomic-level descriptors are defined as[42,43]

$$S_{i;k} = c_k \sum_{j \neq i} \exp\left[-\frac{1}{2}\left(\frac{r_{ij}}{\sigma_k}\right)^2\right] f_{\text{cut}}(r_{ij}) \tag{1}$$

$$V_{i,\alpha;k} = c_k \sum_{j \neq i} \frac{r_{ij}^{\alpha}}{r_{ij}} \exp\left[-\frac{1}{2}\left(\frac{r_{ij}}{\sigma_k}\right)^2\right] f_{\text{cut}}(r_{ij}) \tag{2}$$

$$T_{i,\{\alpha,\beta\};k} = c_k \sum_{j \neq i} \frac{r_{ij}^{\alpha} r_{ij}^{\beta}}{r_{ij}^2} \exp\left[-\frac{1}{2}\left(\frac{r_{ij}}{\sigma_k}\right)^2\right] f_{\text{cut}}(r_{ij}) \tag{3}$$

with r_i and r_j being the Cartesian coordinates of atoms i and j, and $r_{ij} = |\mathbf{r}_j - \mathbf{r}_i|$. α and β represent any of the three x, y, or z directions. The σ_k values define the width of the Gaussian function.[35] The cutoff function

$$f_{\text{cut}}(r_{ij}) = \frac{1}{2}\left[\cos\left(\frac{\pi r_{ij}}{R_{\text{cut}}}\right) + 1\right]$$

smoothly decays an atom's contribution toward zero within a cutoff radius R_{cut}, which was chosen to be 8 Å. c_k is a normalization constant defined as $\left(\frac{1}{\sigma_k \sqrt{2\pi}}\right)^3$.

These descriptors are, however, not invariant under all appropriate transformations, and are therefore not suitable for mapping to a property such as energy. To alleviate this deficiency, a separate step is required which maps the atomic descriptors to a set of structural descriptors, which are defined as[41,42]

$$V_{i,k} = \sqrt{(V_{i,x;k})^2 + (V_{i,y;k})^2 + (V_{i,z;k})^2} \tag{4}$$

$$T'_{i,k} = T_{i,\{x,x\},k}T_{i,\{y,y\},k} + T_{i,\{x,x\},k}T_{i,\{z,z\},k} + T_{i,\{y,y\},k}T_{i,\{z,z\},k} - (T_{i,\{x,y\},k})^2 - (T_{i,\{x,z\},k})^2 - (T_{i,\{y,z\},k})^2 \tag{5}$$

and

$$T''_{i,k} = \det(T_{i,\{\alpha,\beta\},k}) \tag{6}$$

In this work, the potential energy is learned using this procedure. Table 1 indicates the final functional forms of all

Table 1. Final Fingerprint Forms Utilized to Learn Energy or Atomic Forces[a]

property type	no. σ_k	σ_k range (Å)	final fingerprint form
forces (F_i^{α})	8	(1.0, 8.0)	$V_{i,\alpha;k}$
energy (E_I)	20	(1.5, 8.0)	$\{M^1(\sum_{i=1}^N S_{i,k}), M^1(\sum_{i=1}^N V_{i,k}), M^1(\sum_{i=1}^N T_{i,k})\}$

[a]For the property type, the subscripts i and I represent a per-atom or per-structure quantity, respectively, and the superscripts α, β represent two possible Cartesian directions.

descriptors for energy, and forces. Here the function $M^1(X)$ represents the 1st moment of the descriptor components and represents the average value of the atomic environments contained within the system.

Kernel Ridge Regression. After the descriptors have been constructed, we employ Kernel Ridge Regression (KRR) to map them to both the atomic forces, and potential energy as two independent ML models.[41] KRR uses a similarity-based nonlinear kernel to establish a connection between the supplied descriptors and the desired property described as[8,33−36,41]

$$P_X = \sum_Y \alpha_Y \exp\left[-\frac{1}{2}\left(\frac{d_{XY}}{\sigma}\right)^2\right] \tag{7}$$

Here the summation iterates over the number of reference descriptors Y supplied to the model's training set. P represents

Table 2. Al Surface Diffusion Energy Barriers on the (111), (110), and (100) Surfaces, as Computed Using DFT, ML-AGNI, and EAM-V, EAM-L, and EAM-M[a]

mechanism	type	DFT (eV)	ML-AGNI (eV)	EAM-V (eV)	EAM-L (eV)	EAM-M (eV)
(111)						
3-fold hop	hop	0.05	0.03	0.06	0.03	0.03
adatom exchange	exchange	0.72	1.09	0.74	1.05	1.02
(110)						
4-fold hop	hop	0.47	0.33	0.19	0.36	0.30
adatom exchange	exchange	0.53	0.52	0.13	0.25	0.27
(100)						
a	exchange	0.27[55]	0.31	0.30[55]	0.63[55]	0.81[55]
b	exchange	0.63[55]	0.63	0.63[55]	1.00[55]	1.04[55]
c	hop	0.63[55]	0.42	0.46[55]	0.52[55]	0.53[55]
d	exchange	0.68[55]	0.67	0.66[55]	1.20[55]	1.16[55]
e	exchange	0.75[55]	0.72	0.84[55]	1.42[55]	1.60[55]
f	vacancy	0.81[55]	1.25	0.88[55]	1.19[55]	1.05[55]
g	vacancy	0.89[55]	1.03	0.90[55]	1.05[55]	0.95[55]
h	exchange	1.03[55]	0.94	0.94[55]	1.33[55]	1.34[55]
i	exchange	1.22[55]	1.24	1.04[55]	1.38[55]	1.49[55]

[a]The barriers shown below are broken up according to the surface on which the reaction occurs. The letters designating the mechanisms for the (100) surface correspond to the descriptions provided in the Supporting Information.

the property being predicted (total potential energy or atomic forces), with X representing the descriptor, the properties of which are being predicted. d_{XY} represents the euclidean distance between descriptors X and Y, calculated within its hyperspace, and is weighted by a length scale parameter σ. During the model optimization phase, the regression weights α_Y and the length scale σ are calculated through a regularized objective function, which is optimized using a 5-fold cross validation process. The ML-AGNI models used in the remainder of this work were not created here, but were generated as part of previous studies.[35,42] We would like to emphasize that while the cost to generate a single ML model takes no more than a day, the cost to generate a representative data set to train such a model may take many months. Therefore, as ML models grow in popularity over the next decade, the need for diverse sets of data will grow exponentially.

Other Computational Details. *Density Functional Theory Details.* All DFT calculations performed in this work employed the Vienna Ab Initio Simulation Package (VASP).[44,45] The PBE functional[46] was used to predict the electronic exchange-correlation interaction. PAW potentials and plane-wave basis functions, taken up to a kinetic energy of 500 eV, were used,[47] with all projection operators being evaluated in the reciprocal space.

Embedded Atom Method Potentials. Three EAM potentials were used in this work (created by Voter, Liu, and Mishin),[48−50] and are referred to as EAM-V, EAM-L, and EAM-M. EAM-V was chosen because of its previous use in the calculation of several potential energy barriers studied in this work.[51,52] EAM-M was chosen due to its reliability in predicting a plethora of mechanical and thermal properties of Al.[50,53,54] However, the reliability of the model's surface predictions has rarely been studied.[55] Similarly, EAM-L was chosen due to its success in reproducing complex behavior in good agreement with both DFT and experiments.[48−50]

Nudged Elastic Band Calculation Details. The energy barriers of adatom diffusion mechanisms on Al surfaces were calculated using nudged elastic band[56,57] calculations, along with the climbing image method.[58] DFT, EAM, and ML-AGNI

are used to allow for a systematic and consistent comparison between the mechanisms. NEB calculations were performed on five-layer and four-layer slabs, for the (111) and (110) and the (100) surfaces, respectively (though it should be mentioned that both EAM and DFT calculations are performed only for the (111) and (110) surfaces in this work, and all (100) NEB calcculations for DFT and EAM were performed in a previous work). The bottom layer remained fixed in all cases. The NEB routine in the Transition State Tools package was used for DFT calculations. Ionic relaxations were terminated at an energy difference of 10^{-2} eV, and the electronic convergence was considered converged at an energy difference of 10^{-5} eV. All EAM and ML-AGNI NEB calculations were performed using LAMMPS.[59] Owing to the low computational cost of both methods, convergence criteria of 10^{-5} eV/Å for forces and 10^{-8} eV for energy were used. All NEB predictions were calculated with respect to the global (largest) barrier height.

Molecular Dynamics Details. All MD simulations were performed in the canonical ensemble using LAMMPS.[59] The melting temperatures of the (111), (110), and (100) surfaces were calculated using a $2 \times 2 \times 20$ supercell, in which neither the top nor the bottom of the slab was fixed. These sizes allow for thermal effects to dissipate between surface regions, to avoid having such oscillations affect the melting point. The size-dependent melting temperature of (111)−(100) Wulff nanoparticles was also calculated using particles between 1 and 10 nm in diameter.

To study the epitaxial growth of the Al (110) surface, MD simulations were performed, using an initial system size of 224 872 atoms, at 300 K for 25 ns, with deposition occurring for the first 10 ns, and equilibration of the deposited atoms occurring over the final 15 ns. Deposited atoms were randomly spawned from a region approximately 20 Å above the surface, and given random initial velocities, though their velocity component, in the direction normal to the surface, ensured that the atom migrated toward the surface, and not away from it. Atoms were deposited at a rate of $1 \frac{ML}{ns}$, which corresponds to approximately 1 new atom being spawned in the "spawn region" every 100 fs. This deposition rate ensures that atoms will not interact with each other prior to reaching the surface.
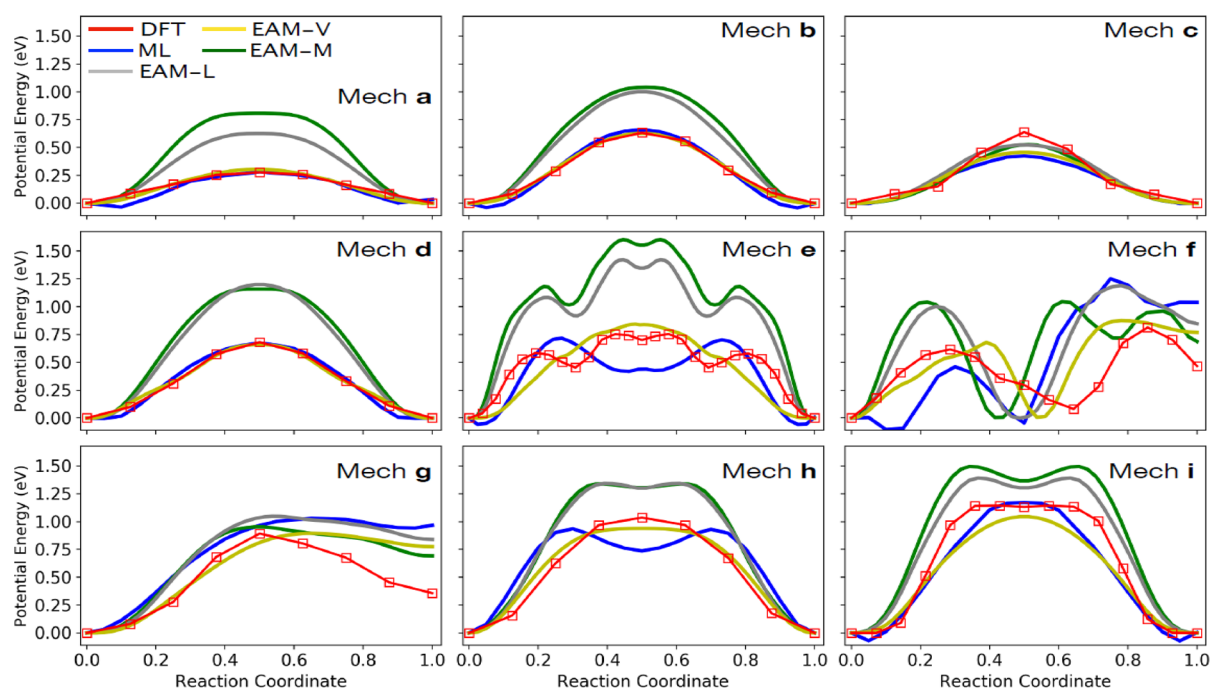
Figure 1. Minimum energy profiles for the Al (100) adatom diffusion mechanisms studied in this work using DFT, ML-AGNI-AGNI, and EAM-V, EAM-C, and EAM-M. All DFT and EAM calculations are taken from the author's previous work.[55] Mechanisms are organized in the order of increasing DFT potential energy barriers.

While this restriction may leave out important physics, the ML-AGNI models cannot simulate gas-phase interactions, and therefore such a limitation is necessary.

RESULTS

Adatom Diffusion on the Al (111) and Al (110) Surfaces. Adatom diffusion on the Al (111) surface is an important surface science phenomena to understand as the Al (111) surface will exist more frequently in nature due to it being the lowest energy surface.[60] However, because the surface is a close-packed surface, the number of unique adatom diffusion mechanisms that can occur is limited due to the energy required to move substrate atoms. The Al (110) surface, while occurring with less frequency than the (111) surface, is still an important surface when it comes to adatom diffusion due to the low packing density between rows, allowing for several competing adatom diffusion pathways.[61]

The physical nature of adatom diffusion on the Al (111) surface paints a very simplistic picture, as only a hop to an adjacent site occurs with any real frequency. That being said, the exchange of the adatom with a substrate atom, pushing the substrate atom up above the surface layer, is also considered. The physical nature of adatom diffusion on the Al (110) surface is more complex,[61] with the reduction in packing density allowing for more potential mechanisms to occur. However, in this work, only two mechanisms are considered: (1) a hop along a row, from one four-fold site to the next, and (2) the exchange between rows, in which an adatom replaces the position of a substrate atom, pushing this atom into the next row to serve as a new adatom.

The potential energy barriers for these mechanisms were studied with three EAM potentials and our ML-AGNI models. All potential energy barriers calculated in this subsection can be found in Table 2. For the simple (111) hop, all potentials show good agreement with both DFT and the experimental

result, with values ranging from 0.03 to 0.06 eV. However, for the case of exchange on the (111) surface, some disagreement exists. EAM-M, EAM-L, and our ML-AGNI models predict a barrier of around 1 eV, while EAM-V and DFT predict a barrier of roughly 0.72. That being said, the take-away from this is that all potentials predict that the exchange on the (111) surface is significantly higher in energy than that of the simple hop.

For the Al (110) surface, a slightly more complex picture exists. For both the exchange and the hop, our calculated DFT results are in good agreement with experimentally observed values. However, for both cases, EAM-V significantly underestimates the potential energy barriers. While both EAM-L and EAM-M show decent agreement with the DFT predicted value of the hop mechanisms, they both significantly underestimate the barrier for the exchange mechanism. For both cases, our ML-AGNI models show the same level of agreement for the hop mechanisms that EAM-M and EAM-L show, but perform much better when estimating the barrier for the exchange mechanism, predicting a nearly identical result.

Adatom Diffusion on the Al (100) Surface. While the Al (111) and (110) surfaces are relatively simplistic in terms of the physical complexity of the pathways in which adatom diffusion can take, self-diffusion on the (100) surface is not as restricted.[62,63] For a variety of metals, such as Al, Pt, and Pd, the adatom's lowest-energy diffusion pathway is that of an atomic exchange mechanism[64] in which an adatom takes the place of a surface atom, thereby pushing the surface atom onto the surface. This is in stark contrast to metals such as Cu and Rh, in which the adatom diffuses through a simple (and intuitive) hop between 4-fold sites.[65] This is in stark contrast to both the Al (111) in which an adatom hop is universally lower in energy than an exchange process, as well as the Al (110) surface in which only a few diffusion pathways are even possible, due to the physical structure of the surface.

Furthermore, a variety of nontrivial low-energy diffusion mechanisms exist in the case of the Al (100) surface, many with unique physical differences.[51,52,55,64,66,67] Previous studies have also shown that many vacancy-based mechanisms[51,52,55] have similar energy barriers to that of the intuitive hop.

Here we validate our ML-AGNI force and energy models on nine previously studied Al (100) adatom diffusion mechanisms.[55] These diffusion pathways involve processes such as atomic exchange, hopping, and vacancy-formation, all employing the same initial geometry of a single adatom on an otherwise clean surface. The physical nature of these nine mechanisms is described in detail both in our previous work[55] and in the Supporting Information. Detailed illustrations of all mechanisms can be found in the Supporting Information.

The ML-AGNI force and energy models were used to predict the MEPs of all nine (100) mechanisms. The calculated diffusion barriers can be found in both Table 2 and Figure 1, while statistical metrics used to judge a given model's performance can be found in Table 3. Overall, the ML-

Table 3. Statistical Metrics Used to Judged All Force Field's Performance on the Various Diffusion Profile Barriers, as Well as the Melting Temperatures Calculated in This Work[a]

statistical metrics	ML-AGNI	EAM-V	EAM-L	EAM-M
E_a (eV)				
RMSE	0.18	0.16	0.33	0.38
σ	0.17	0.14	0.26	0.30
r^2	0.88	0.89	0.82	0.71
p_{KS}	0.88	0.88	0.13	0.12
T_m (K)				
RMSE	66.8	173.34	158.31	198.07
σ	58.2	132.90	97.88	79.15
r^2	0.94	0.81	0.97	0.91
p_{KS}	0.96	0.05	0.21	0.05

[a]p_{KS} is used to designate the p-value from the Kolmogorov−Smirnov test. Each block corresponds to a specific property. The units of each value presented here correspond to the units used for each property (eV for the MEPs, and K for the melting temperature). Activation energies statistics are calculated with respect to DFT, and melting temperature statistics are calculated with respect to the experimental values.

AGNI results align extremely well with DFT. The ML-AGNI transition state energies yield an RMSE of 0.21 eV, compared to an RMSE of 0.33 and 0.35 eV for EAM-L and EAM-M, respectively. While this 0.21 eV RMSE is higher than the 0.1 eV of EAM-V, this difference can be attributed to the ML-AGNI prediction on mechanism f, which is 0.44 eV off compared to the DFT prediction. The ML-AGNI RMSE, compared to that of DFT, on all mechanisms not including mechanism f, is 0.08, which is 0.02 eV lower than the RMSE of 0.1 of EAM-V on all mechanisms not including mechanism f.

Kolmogorov−Smirnov p-values[68] were also calculated using all potential energy barriers studied in this work, and can be found in Table 3. Both AGNI and EAM-V produce a p-value of 0.88, indicating good agreement with the corresponding DFT values. EAM-L and EAM-M yield p-values of 0.13 and 0.12, respectively, further highlighting their struggles to accurately predict the diffusion barriers. These results, combined with the other statistical metrics discussed previously indicate that the

ML-AGNI models can reliably predict the kinetics of adatom/vacancy diffusion profiles on the Al (100) surface.

Predicting the Melting Temperature of Al Surfaces and Nanoparticles. The melting behavior of aluminum surfaces varies greatly, as the difference in packing densities leads to a wide range of melting temperatures.[69,70] Experimental observations indicate that, between the low-index (111), (110), and (100) surfaces, a difference in melting temperature of nearly 300 K exists.[71] The (111) and (100) surfaces exhibit melting at the bulk melting temperature of between 900 and 950 K. However, due to the packing density, the (110) surface has a melting temperature of between 600 and 800 K.[72] This disparity becomes more complex when one moves from a slab to a nanoparticle, with small particles showing melting temperatures around 400 K lower than that of the bulk melting temperature. These temperatures vary drastically as a function of the small particle size.[70,73]

Recently, ML methods have been used to accurately predict the structures of liquids,[74] as well as correctly reproduce the bulk melting temperatures of metals.[75] However, ML methods have not been widely used to study how various surface environments affect the melting temperature. To this end, the melting temperature of the Al (111), (110), and (100) surfaces was calculated using three EAM potentials, and our ML-AGNI models. The calculated melting temperatures from this work can be found in Figure 4, and the statistical metrics used to judge a given model's performance can be found in Table 3. Figure 2 shows, in the top row, the potential energy as a function of time at different temperatures for each case considered. The bottom row corresponds to the Lindemann index, calculated for all cases considered. From the EAM potential's perspective, there is no consensus among the potentials. EAM-V underestimates all melting temperatures, sometimes by several hundred degrees Kelvin, while EAM-M generally overestimates all melting temperatures, though is often closer to the experimentally observed melting temperature. EAM-L seems to be the robust EAM potential when predicting the melting temperature of clean Al surfaces, showing excellent agreement with respect to experiments. The ML-AGNI models predict a melting temperature of approximately 950, 850, and 750 K for the (111), (100), and (110) surfaces, respectively. These results are in good overall agreement with experiments, and are only out-performed, on the whole, by EAM-L.

The melting temperature of several Al nanoparticles was also considered in this work. It has been observed experimentally that the melting temperature of Al nanoparticles changes dramatically as a function of nanoparticle size, with particles 1 nm in diameter showing a melting temperature nearly 400 K less than that of a 10 nm particle, which has a melting temperature close to that of bulk Al. To this end, MD simulations were performed, using all three EAM potentials and our ML-AGNI models. Figure 3 details the calculated Lindemann index for four nanoparticles, all of different sizes.

As was the case with the clean surfaces, there is no consensus among the EAM potentials, with dramatic differences in the melting temperatures being observed. Interestingly, the same trend exists, with EAM-M overestimating the melting temperature, and EAM-V generally underestimating (expect for the 1 nm case in which it slightly overestimates the melting temperature). While EAM-V performs well for small particles, it performs poorly for larger ones, with the opposite being true for EAM-M and EAM-L. Therefore, there is no
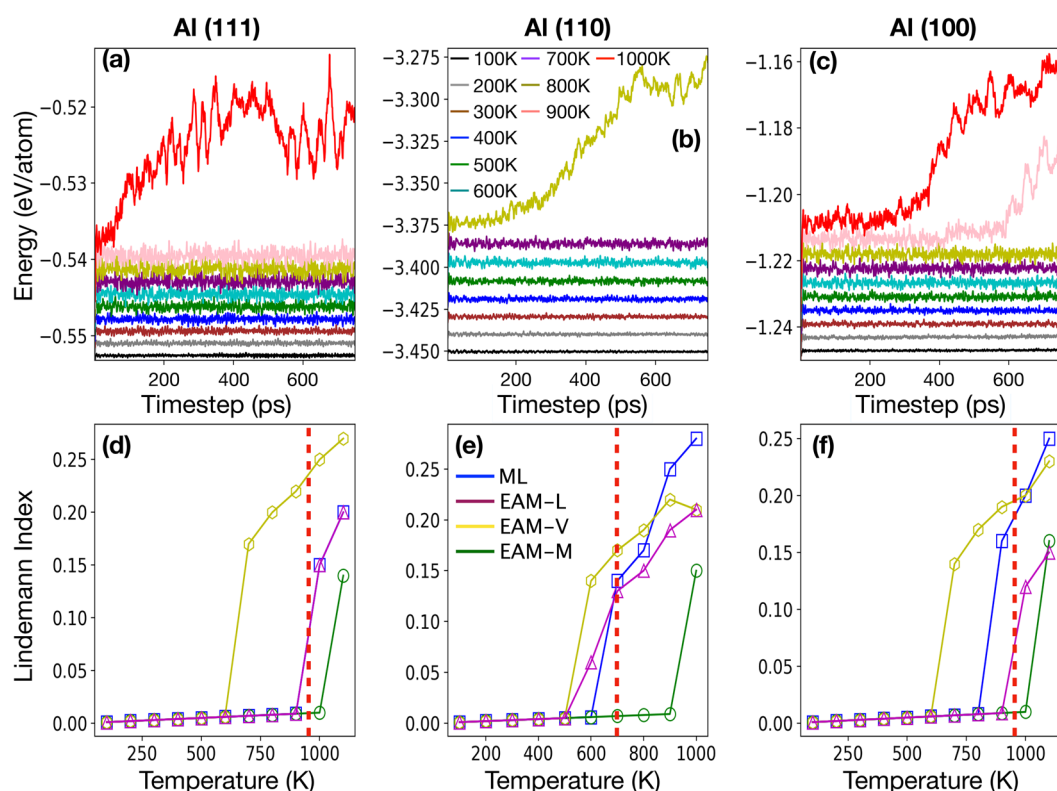
Figure 2. (Top) Potential energy, as a function of time step during an MD simulation, for (a) Al (111) surface, (b) Al (110) surface, (c) Al (100) surface. Colors correspond to a particular temperature, and are the same throughout all top-row plots. (Bottom) Lindemann index, used to study the structural order of each system, calculated for the (d) Al (111) surface, (e) Al (110) surface, (f) Al (100) surface. Vertical red, dotted lines correspond to the experimentally predicted melting temperature.
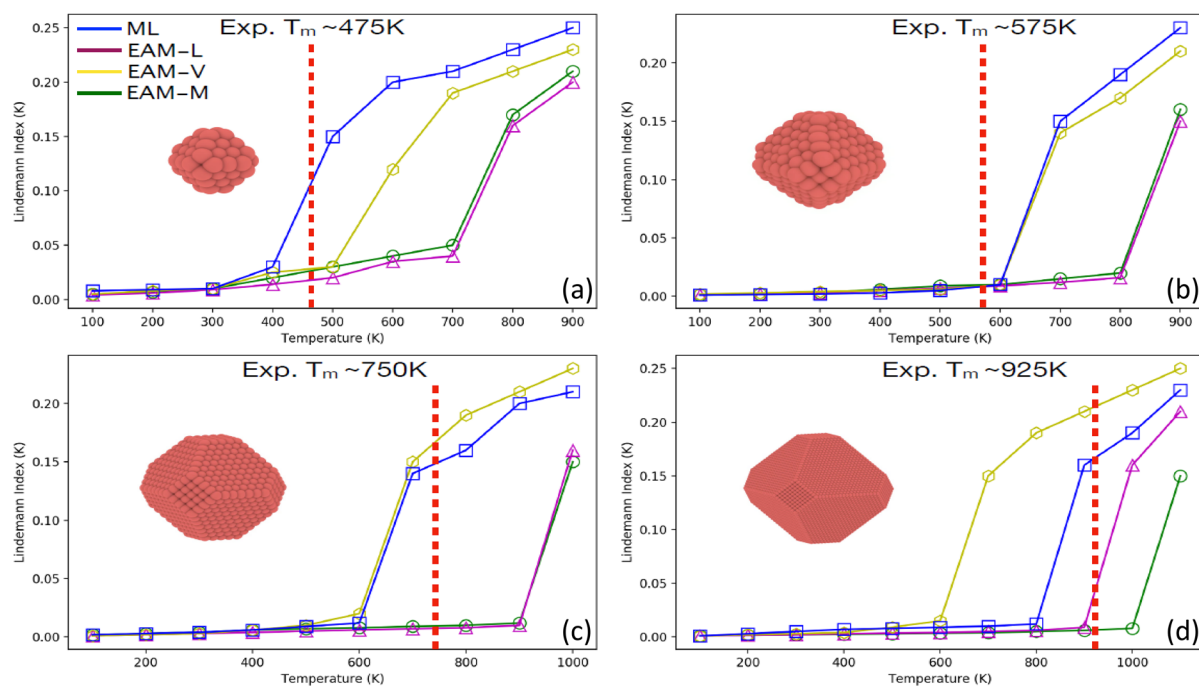

Figure 3. Lindemann index, used to study the structural order of each system, calculated for the (a) Al 1 nm particle, (b) 2 nm particle, (c) 4 nm particle, and (d) 10 nm particle. Vertical red, dotted lines correspond to the experimentally predicted melting temperature.

single EAM potential one can use to accurately capture the trend correctly, with respect to experiments.

Our ML-AGNI models outperform all considered EAM potentials on average, accurately capturing the trend in which

the nanoparticle size affects the melting temperature by up to 500 K. The ML-AGNI models accurately predict the melting temperature of the 1 nm particle to be approximately 450 K. The ML-AGNI models predict roughly the same temperature
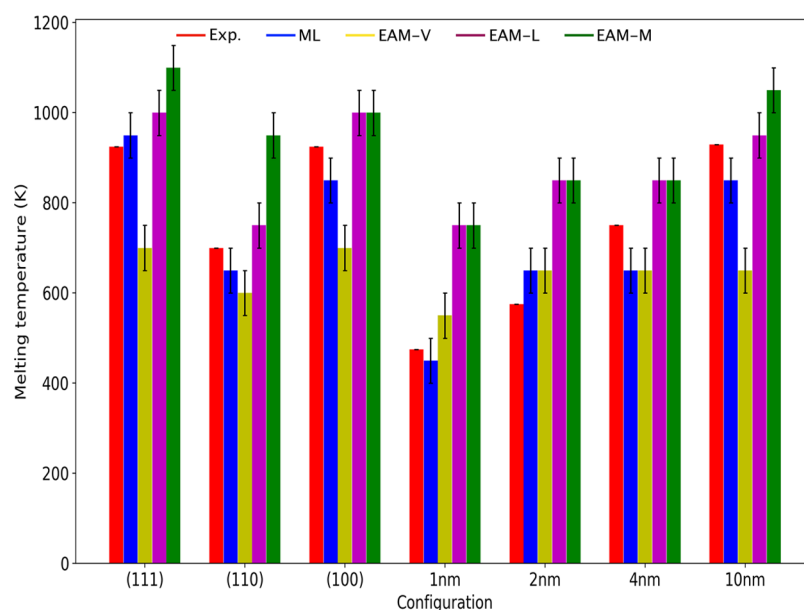
Figure 4. Melting temperatures for all configurations studied in this work. Colors correspond to the prediction method. Error bars correspond to the assumed error in a given calculation (experimental results are given as zero error, as the error is unknown, whereas the MD simulation error is given as 50 K, as this is the error assumed given the Lindemann index calculations.)
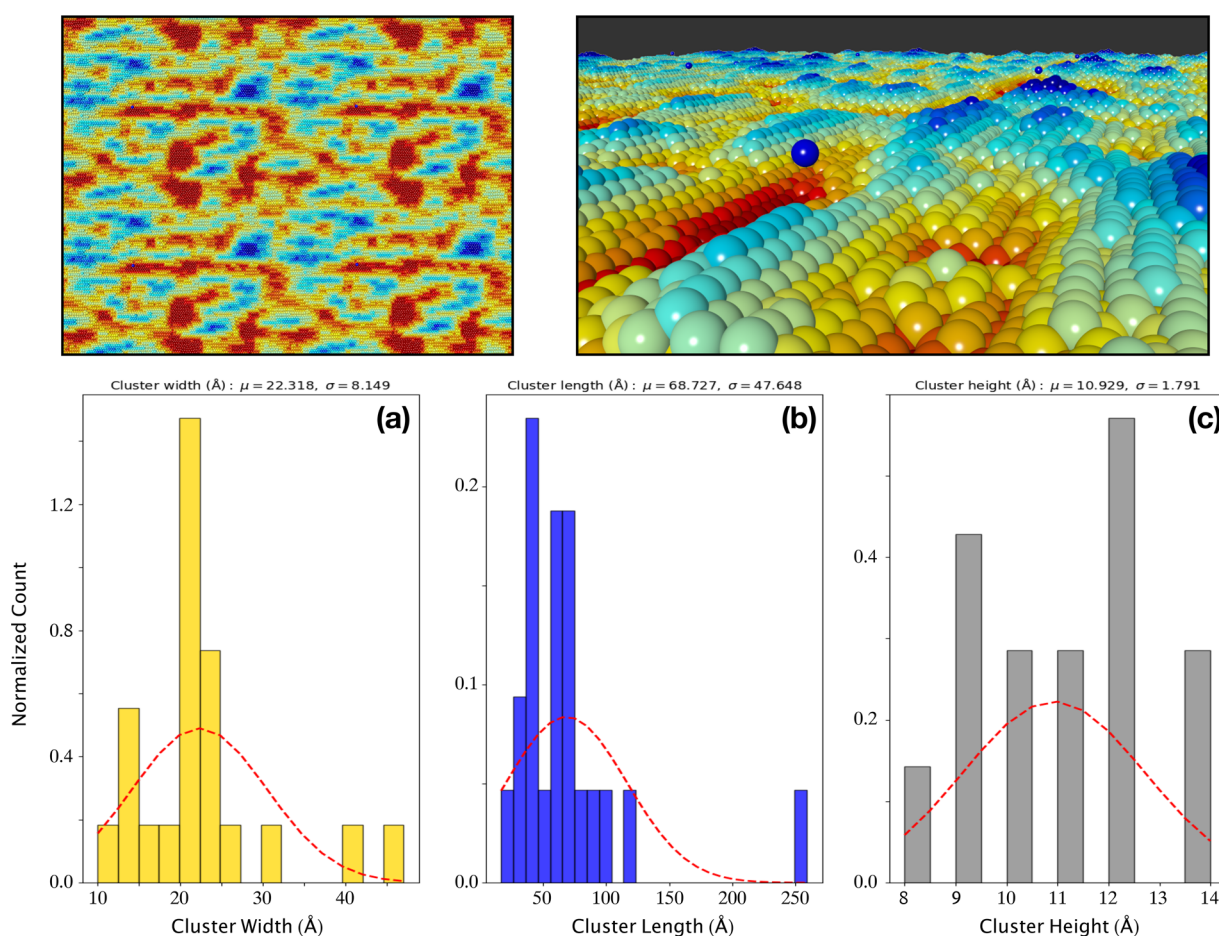

Figure 5. (Top) A 2 × 2 replicated top-down view, shown on the left, and a 3 × 3 replicated perspective view, shown on the right, of the epitaxial growth of the Al (110 surface. Colors corresponding to the z-position of an atom, with red representing smaller, and blue representing a larger z-position. (Bottom) Normalized histograms for the (a) width, (b) length, and (c) height, of the deposited clusters on the surface after both deposition and equilibration had occurred.) The red dashed lines in histograms a, b, and c represent normalized Gaussian functions fit to the underlying histogram data and are used to calculate the values shown above each plot.

for the 2 and 4 nm particle of 650 K, even though the experimentally observed melting temperatures are 575 and 750 K, respectively. However, the best-performing EAM potential for the smaller nanoparticles, EAM-V, predicts a nearly identical melting temperature for both particles. Finally, the ML-AGNI models predict a melting temperature of roughly 850 K for the 10 nm particle, approximately 75 K lower than the experimentally observed melting temperature. Over the spectrum of nanoparticle sizes, our ML-AGNI models provide the most reliable melting temperature predictions compared to several popular EAM potentials for Al.

Statistical metrics used to compare the various model's predicted melting temperatures can be found in Table 3. All three EAM potentials yield an RMSE of at least 150 K, when compared to experiments, while our AGNI models have an RMSE of only 66 K. This implies that our AGNI models are nearly 200−300% more accurate when compared to the EAM models, when predicting the melting temperature of many complex surface/particle environments. This difference in predicted melting temperature is further exemplified when one looks at the p-values calculated via the Kolmogorov−Smirnov test. All three EAM potentials have p-values smaller than 0.25, with two potentials yielding values lower than 0.06 (the typical threshold for statistical significance is generally between 0.01 and 0.05). Our AGNI models have a calculated p-value of 0.96 when compared to the experimental melting temperatures, indicating that the AGNI values share significant statistical relevance with the experimentally observed melting temperatures.

Expitaxial Growth on the Al (110) Surface. AFM images of epitaxial growth on the Al (110) surface,[76] via atomic-layer deposition, provides us with quantitative values in which to benchmark our ML-AGNI models against. At 300 K pyramidal clusters form on the surface with lengths and heights approximately three and six times smaller than their width, respectively. While the MD simulations performed in this section will still not reach the time and length scales observed in experiments, the time and length-scales used can provide exact qualitative measurements; the size of the pyramidal clusters may be an order of magnitude smaller via MD, but the height−width−length relationship can match experimental observations.

It can be seen from Figure 5 that the height−width−length relationship obtained from the ML-AGNI MD simulations match extremely well with experimental observations. The width, height, and length of clusters were calculated as the average of all clusters present at the end of the MD simulation. The height, specifically, was calculated as the distance from the nearest monolayer atom to the top of a given cluster. The measured average cluster width was measured as 22.31 Å, almost exactly three times smaller than the 68.72 Å width. The average cluster height was calculated to be 10.92 Å, in near perfect agreement with the experimental observation of the cluster height to width ratio of 6:1.[76]

To build upon the agreement with experiments, Figure 5 shows the top-down and perspective views of the Al (110) surface at the end of the MD simulation. AFM images indicate long, tube-shaped clusters spread throughout the surface, with small clusters and valleys filling the remaining space.[76] Figure 5 indicates similar surface features, obtained via the MD simulations, being present. The perspective view of the final ML-AGNI simulated structure also clearly shows pyramidal structures being present, the width−length ratio of which resembles the long tube-like shape observed in experiments.

CONCLUSION

In this work, ML-AGNI force and energy models were used to study a multitude of surface phenomena of aluminum. Here, we further extend the scope of previous ML-AGNI works by tackling simulations of increasingly complex physical systems, and significantly larger time and length scales than had been previously considered. The various ML-AGNI models were validated by accurately reproducing the MEPs of a plethora of defect diffusion mechanisms on several low-index Al surfaces, accurately reproducing the correct melting temperatures of Al surfaces and predicting the size-dependent melting temperature of Al nanoparticles, as well as accurately reproducing experimental observations of the cluster shapes and sizes during epitaxial growth, via atomic-layer deposition, of the Al(110) surface.

The ML-AGNI calculations presented in this chapter show a clear improvement in the prediction of surface phenomena over many commonly used EAM potentials. The ML-AGNI models presented here also, purposefully, do not contain reference data for all of the environments studied, indicating their extrapolative power. Using ML models, with the accuracy of DFT and the speed of classical/semiempirical models, allows us to reliably study phenomena that are impractical to be computed using DFT. This work adds another layer of validation that ML models can make reliable predictions over multiple length and time scales and solidifies ML as a important tool in the study of atomic and nanoscale surface problems.

ASSOCIATED CONTENT

ⓈI Supporting Information

The Supporting Information is available free of charge at https://pubs.acs.org/doi/10.1021/acs.jpcc.0c05512.

> Series of snapshots throughout the molecular dynamics simulation of epitaxial growth on the Al (110) surface (MOV)

> Detailed description of the fingerprinting process; explanation of the physical nature of the Al (100) adatom diffusion mechanisms (PDF)

AUTHOR INFORMATION

Corresponding Author

James Chapman − *School of Materials Science & Engineering, Georgia Institute of Technology, Atlanta, Georgia 30332, United States;* ⓞ orcid.org/0000-0003-3484-9726; Email: jchapman48@gatech.edu

Author

Rampi Ramprasad − *School of Materials Science & Engineering, Georgia Institute of Technology, Atlanta, Georgia 30332, United States;* ⓞ orcid.org/0000-0003-4630-1565

Complete contact information is available at: https://pubs.acs.org/10.1021/acs.jpcc.0c05512

Notes

The authors declare no competing financial interest.
The raw DFT data used to generate all ML models used in this work is available to download from khazana.gatech.edu. All ML models used in this work can be found for download, or used

directly though our web platform located at khazana.gatech.e-du.

■ REFERENCES

(1) Johnson, R.; Hultqvist, A.; Bent, S. A brief review of atomic layer deposition: from fundamentals to applications. *Mater. Today* **2014**, *17*, 236−246.

(2) Zhang, Z.; Lagally, M. G. Atomistic Processes in the Early Stages of Thin-Film Growth. *Science* **1997**, *276*, 377−383.

(3) Recoules, V.; Renaudin, P.; Clérouin, J.; Noiret, P.; Zérah, G. Electrical conductivity of hot expanded aluminum: Experimental measurements and ab initio calculations. *Phys. Rev. E: Stat. Phys., Plasmas, Fluids, Relat. Interdiscip. Top.* **2002**, *66*, 056412.

(4) Davis, J. *Corrosion of Aluminum and Aluminum Alloys*; ASM International 1999,.

(5) Scamans, G.; Birbilis, N.; Buchheit, R. In *Shreir's Corrosion*, 1st ed.; Richardson, T., Ed.; Elsevier: Netherlands, 2010; pp 1974−2010.

(6) Klaiman, K.; Ortega, D. L.; Garnache, C. Consumer preferences and demand for packaging material and recyclability. *Resources, Conservation and Recycling* **2016**, *115*, 1−8.

(7) Liu, G.; Müller, D. B. Addressing sustainability in the aluminum industry: a critical review of life cycle assessments. *J. Cleaner Prod.* **2012**, *35*, 108−117.

(8) Botu, V.; Chapman, J.; Ramprasad, R. A study of adatom ripening on an Al (111) surface with machine learning force fields. *Comput. Mater. Sci.* **2017**, *129*, 332−335.

(9) Rassoulinejad-Mousavi, S. M.; Zhang, Y. Interatomic Potentials Transferability for Molecular Simulations: A Comparative Study for Platinum, Gold and Silver. *Sci. Rep.* **2018**, *8*, 2424.

(10) Grochola, G.; Russo, S. P.; Snook, I. K. On fitting a gold embedded atom method potential using the force matching method. *J. Chem. Phys.* **2005**, *123*, 204719.

(11) O'Brien, C. J.; Barr, C. M.; Price, P. M.; Hattar, K.; Foiles, S. M. Grain boundary phase transformations in PtAu and relevance to thermal stabilization of bulk nanocrystalline metals. *J. Mater. Sci.* **2018**, *53*, 2911−2927.

(12) Zhou, X. W.; Johnson, R. A.; Wadley, H. N. G. Misfit-energy-increasing dislocations in vapor-deposited CoFeÕNiFe multilayers. *Phys. Rev. B: Condens. Matter Mater. Phys.* **2004**, *60*, 144113.

(13) Foiles, S. M.; Baskes, M. I.; Daw, M. S. Embedded-atom-method functions for the fcc metals Cu, Ag, Au, Ni, Pd, Pt, and their alloys. *Phys. Rev. B: Condens. Matter Mater. Phys.* **1988**, *37*, 10378.

(14) Hohenberg, P.; Kohn, W. Inhomogeneous electron gas. *Phys. Rev.* **1964**, *136*, B864−B871.

(15) Kohn, W.; Sham, L. J. Self-consistent equations including exchange and correlation effects. *Phys. Rev.* **1965**, *140*, A1133−A1138.

(16) Jones, R. O. Density functional theory: Its origins, rise to prominence, and future. *Rev. Mod. Phys.* **2015**, *87*, 897−923.

(17) Jones, J. E.; Chapman, S. On the determination of molecular fields. *Proc. R. Soc. London A* **1924**, *106*, 463−477.

(18) Daw, M. S.; Baskes, M. I. Embedded-atom method: Derivation and application to impurities, surfaces, and other defects in metals. *Phys. Rev. B: Condens. Matter Mater. Phys.* **1984**, *29*, 6443−6453.

(19) Daw, M. S.; Foiles, S. M.; Baskes, M. I. The embedded-atom method: a review of theory and applications. *Mater. Sci. Rep.* **1993**, *9*, 251−310.

(20) Tersoff, J. New empirical approach for the structure and energy of covalent systems. *Phys. Rev. B: Condens. Matter Mater. Phys.* **1988**, *37*, 6991−7000.

(21) Bazant, M. Z.; Kaxiras, E.; Justo, J. F. Environment-dependent interatomic potential for bulk silicon. *Phys. Rev. B: Condens. Matter Mater. Phys.* **1997**, *56*, 8542−8552.

(22) van Duin, A. C. T.; Dasgupta, S.; Lorant, F.; Goddard, W. A. ReaxFF: A Reactive Force Field for Hydrocarbons. *J. Phys. Chem. A* **2001**, *105*, 9396−9409.

(23) Bianchini, F.; Kermode, J. R.; Vita, A. D. Modelling defects in Ni−hAl with EAM and DFT calculations. *Modell. Simul. Mater. Sci. Eng.* **2016**, *24*, 045012.

(24) Gasteiger, J.; Zupan, J. Neural Networks in Chemistry. *Angew. Chem., Int. Ed. Engl.* **1993**, *32*, 503−527.

(25) Sumpter, B. G.; Getino, C.; Noid, D. W. Theory and Applications of Neural Computing in Chemical Science. *Annu. Rev. Phys. Chem.* **1994**, *45*, 439−481.

(26) Rajan, K. Materials informatics. *Mater. Today* **2005**, *8*, 38−45.

(27) Ramprasad, R.; Batra, R.; Pilania, G.; Mannodi-Kanakkithodi, A.; Kim, C. Machine Learning and Materials Informatics: Recent Applications and Prospects. *npj Comput. Mater.* **2017**, *54*, No. 0056-5, DOI: 10.1038/s41524-017-0056-5.

(28) Mannodi-Kanakkithodi, A.; Chandrasekaran, A.; Kim, C.; Huan, T. D.; Pilania, G.; Botu, V.; Ramprasad, R. Scoping the polymer genome: A roadmap for rational polymer dielectrics design and beyond. *Mater. Today* **2018**, *21*, 785−796.

(29) Kim, C.; Chandrasekaran, A.; Huan, T. D.; Das, D.; Ramprasad, R. Polymer Genome: A Data-Powered Polymer Informatics Platform for Property Predictions. *J. Phys. Chem. C* **2018**, *122*, 17575−17585.

(30) Pilania, G.; Wang, C.; Jiang, X.; Rajasekaran, S.; Ramprasad, R. Accelerating materials property predictions using machine learning. *Sci. Rep.* **2013**, *3*, 2810.

(31) Huan, T. D.; Mannodi-Kanakkithodi, A.; Ramprasad, R. Accelerated materials property predictions and design using motif-based fingerprints. *Phys. Rev. B: Condens. Matter Mater. Phys.* **2015**, *92*, No. 014106, DOI: 10.1103/PhysRevB.92.014106.

(32) Mannodi-Kanakkithodi, A.; Pilania, G.; Huan, T. D.; Lookman, T.; Ramprasad, R. Machine learning strategy for the accelerated design of polymer dielectrics. *Sci. Rep.* **2016**, *6*, 20952.

(33) Botu, V.; Ramprasad, R. Adaptive machine learning framework to accelerate ab initio molecular dynamics. *Int. J. Quantum Chem.* **2015**, *115*, 1074−1083.

(34) Botu, V.; Ramprasad, R. Learning scheme to predict atomic forces and accelerate materials simulations. *Phys. Rev. B: Condens. Matter Mater. Phys.* **2015**, *92*, 094306.

(35) Botu, V.; Batra, R.; Chapman, J.; Ramprasad, R. Machine learning force fields: Construction, validation, and outlook. *J. Phys. Chem. C* **2017**, *121*, 511−522.

(36) Huan, T. D.; Batra, R.; Chapman, J.; Krishnan, S.; Chen, L.; Ramprasad, R. A universal strategy for the creation of machine learning based atomistic force fields. *npj Comput. Mater.* **2017**, *3*, 37.

(37) Behler, J.; Parrinello, M. Generalized Neural-Network Representation of High- Dimensional Potential-Energy Surfaces. *Phys. Rev. Lett.* **2007**, *98*, 146401.

(38) Bartók, A. P.; Csányi, G. Gaussian Approximation Potentials: A Brief Tutorial Introduction. *Int. J. Quantum Chem.* **2015**, *115*, 1051−1057.

(39) Chmiela, S.; Tkatchenko, A.; Sauceda, H. E.; Poltavsky, T.; Schutt, K. T.; Muller, K. R. Machine learning of accurate energy-conserving molecular force fields. *Sci. Adv.* **2017**, *3*, e1603015.

(40) Huan, T. D.; Batra, R.; Chapman, J.; Kim, C.; Chandrasekaran, A.; Ramprasad, R. Iterative-Learning Strategy for the Development of Application-Specific Atomistic Force Fields. *J. Phys. Chem. C* **2019**, *123*, 20715.

(41) Chapman, J.; Batra, R.; Ramprasad, R. Machine learning models for the prediction of energy, forces, and stresses for Platinum. *Comput. Mater. Sci.* **2020**, *174*, 109483.

(42) Batra, R.; Tran, H. D.; Kim, C.; Chapman, J.; Chen, L.; Chandrasekaran, A.; Ramprasad, R. General Atomic Neighborhood Fingerprint for Machine Learning-Based Methods. *J. Phys. Chem. C* **2019**, *123*, 15859−15866.

(43) Chandrasekaran, A.; Kamal, D.; Batra, R.; Kim, C.; Chen, L.; Ramprasad, R. Solving the electronic structure problem with machine learning. *npj Computational Materials* **2019**, *5*, 22.

(44) Kresse, G.; Furthmüller, J. Efficient iterative schemes for ab initio total energy calculations using a plane-wave basis set. *Phys. Rev. B: Condens. Matter Mater. Phys.* **1996**, *54*, 11169.

(45) Kresse, G.; Joubert, D. From ultrasoft pseudopotentials to the projector augmented wave method. *Phys. Rev. B: Condens. Matter Mater. Phys.* **1999**, *59*, 1758.

(46) Perdew, J. P.; Burke, K.; Wang, Y. Generalized gradient approximation for the exchange-correlation hole of a many electron system. *Phys. Rev. B: Condens. Matter Mater. Phys.* **1996**, *54*, 16533.

(47) Blöchl, P. E. Projector augmented wave method. *Phys. Rev. B: Condens. Matter Mater. Phys.* **1994**, *50*, 17953.

(48) Voter, A.; Chen, S. Accurate interatomic potentials for Ni, Al, and Ni3Al. *Mater. Res. Soc.* **1986**, *82*, 175.

(49) Liu, X.; Ercolessi, F.; Adams, J. Aluminium interatomic potential from density functional theory calculations with improved stacking fault energy. *Modell. Simul. Mater. Sci. Eng.* **2004**, *12*, 665.

(50) Zope, R.; Mishin, Y. Interatomic potentials for atomistic simulations of the Ti-Al system. *Phys. Rev. B: Condens. Matter Mater. Phys.* **2003**, *68*, No. 024102, DOI: 10.1103/PhysRevB.68.024102.

(51) Henkelman, G.; Jònsson, H. A dimer method for finding saddle points on high dimensional potential surfaces using only first derivatives. *J. Chem. Phys.* **1999**, *111*, 7010−7022.

(52) Henkelman, G.; Jònsson, H. Long time scale kinetic Monte Carlo simulations without lattice approximation and predefined event table. *J. Chem. Phys.* **2001**, *115*, 9657−9666.

(53) Wang, J.; Horsfield, A.; Lee, P.; Brommer, P. Heterogeneous nucleation of solid Al from the melt by Al3Ti: Molecular dynamics simulations. *Phys. Rev. B: Condens. Matter Mater. Phys.* **2010**, *82*, No. 144203, DOI: 10.1103/PhysRevB.82.144203.

(54) Levchenko, E.; Evteev, A.; Löwisch, G.; Belova, I.; Murch, G. Molecular dynamics simulation of alloying in a Ti-coated Al nanoparticle. *Intermetallics* **2012**, *22*, 193.

(55) Chapman, J.; Batra, R.; Uberuaga, B.; Pilania, G.; Ramprasad, R. A comprehensive computational study of adatom diffusion on the aluminum (100) surface. *Comput. Mater. Sci.* **2019**, *158*, 353−358.

(56) Jònsson, H.; Mills, G.; Jacobsen, K. W. Nudged elastic band method for finding minimum energy paths of transitions. Classical and Quantum. *Dynamics in Condensed Phase Simulations* **1997**, *50*, 385.

(57) Jònsson, H.; Henkelman, G. Improved tangent estimate in the nudged elastic band method for finding minimum energy paths and saddle points. *J. Chem. Phys.* **2000**, *113*, 9978.

(58) Henkelman, G.; Uberuaga, B. P.; Jonsson, H. A climbing image nudged elastic band method for finding saddle points and minimum energy paths. *J. Chem. Phys.* **2000**, *113*, 9901.

(59) Plimpton, S. Fast parallel algorithms for short-range molecular dynamics. *J. Comput. Phys.* **1995**, *117*, 1−19.

(60) Valkealahti, S.; Manninen, M. Diffusion on aluminum-cluster surfaces and the cluster growth. *Phys. Rev. B: Condens. Matter Mater. Phys.* **1998**, *57*, 15533−15540.

(61) Gravil, P.; Holloway, S. Exchange mechanisms for self-diffusion on aluminium surfaces. *Surf. Sci.* **1994**, *310*, 267−272.

(62) Kellogg, G. Field ion microscope studies of single-atom surface diffusion and cluster nucleation on metal surfaces. *Surf. Sci. Rep.* **1994**, *21*, 1−88.

(63) Yu, B. D.; Scheffler, M. Physical origin of exchange diffusion on fcc(100) metal surfaces. *Phys. Rev. B: Condens. Matter Mater. Phys.* **1997**, *56*, R15569−R15572.

(64) Feibelman, P. Diffusion path for an Al adatom on Al(001). *Phys. Rev. Lett.* **1990**, *65*, 729−732.

(65) Chang, C. M.; Wei, C. M. Self-diffusion of Adatoms and Dimers on fcc (100) Surfaces. *Chin. J. Phys.* **2005**, *43*, 169−175.

(66) Gravil, P.; Holloway, S. Exchange mechanisms for self-diffusion on aluminum surfaces. *Surf. Sci.* **1994**, *310*, 267−272.

(67) Stumpf, R.; Scheffler, M. Ab initio calculations of energies and self-diffusion on flat and stepped surfaces of Al and their implications on crystal growth. *Phys. Rev. B: Condens. Matter Mater. Phys.* **1996**, *53*, 4958−4973.

(68) Massey, F. J. The Kolmogorov-Smirnov Test for Goodness of Fit. *J. Am. Stat. Assoc.* **1951**, *46*, 68−78.

(69) Sun, J.; Simon, S. The melting behavior of aluminum nanoparticles. *Thermochim. Acta* **2007**, *463*, 32−40. Chemical Thermodynamics and Thermal Analysis.

(70) Eastment, R. M.; Mee, C. H. B. Work function measurements on (100), (110) and (111) surfaces of aluminium. *J. Phys. F: Met. Phys.* **1973**, *3*, 1738−1745.

(71) Stoltze, P.; Nørskov, J. K.; Landman, U. Disordering and Melting of Aluminum Surfaces. *Phys. Rev. Lett.* **1988**, *61*, 440−443.

(72) Pedemonte, L.; Bracco, G.; Robin, A.; Heiland, W. Residual order within the molten Al(110) surface layer. *Phys. Rev. B: Condens. Matter Mater. Phys.* **2002**, *65*, 245406.

(73) Fedorov, A. V.; Shulgin, A. V.; Lavruk, S. A. Description of melting of aluminum nanoparticles. *Combust., Explos. Shock Waves* **2016**, *52*, 457−462.

(74) Sivaraman, G.; Krishnamoorthy, A. N.; Baur, M.; Holm, C.; Stan, M.; Csányi, G.; Benmore, C.; Vázquez-Mayagoitia, Á. Machine-learned interatomic potentials by active learning: amorphous and liquid hafnium dioxide. *npj Computational Materials* **2020**, *6*, 104.

(75) Smith, J. S.; Nebgen, B.; Mathew, N.; Chen, J.; Lubbers, N.; Burakovsky, L.; Tretiak, S.; Nam, H. A.; Germann, T.; Fensin, S.; Barros, K. *Automated discovery of a robust interatomic potential for aluminum.* arXiv e-prints ver. 2, Aug 24, 2020, https://arxiv.org/abs/2003.04934.

(76) Buatier de Mongeot, F.; Zhu, W.; Molle, A.; Buzio, R.; Boragno, C.; Valbusa, U.; Wang, E. G.; Zhang, Z. Nanocrystal Formation and Faceting Instability in Al(110) Homoepitaxy: True Upward Adatom Diffusion at Step Edges and Island Corners. *Phys. Rev. Lett.* **2003**, *91*, 016102.